

# The Gabor Frame as a Discretization for the 2D Transverse-Electric Scattering-Problem Domain Integral Equation

Roeland J. Ditz\* and Martijn C. Van Beurden

**Abstract**—We apply the Gabor frame as a projection method to numerically solve a 2D transverse-electric-polarized domain-integral equation for a homogeneous medium. Since the Gabor frame is spatially as well as spectrally very well convergent, it is convenient to use for solving a domain integral equation. The mixed spatial and spectral nature of the Gabor frame creates a natural and fast way to Fourier transform a function. In the spectral domain we employ a coordinate scaling to smoothen the branchcut found in the Green function. We have developed algorithms to perform multiplication and convolution efficiently, scaling as  $O(N \log N)$  on the number of Gabor coefficients, yielding an overall algorithm that also scales as  $O(N \log N)$ .

## 1. INTRODUCTION

Numerical modeling of electromagnetic scattering by dielectric objects is important in many fields. To efficiently design and optimize many types of optical structures, accurate and fast numerical schemes are required to characterize their optical properties. We are interested in modeling the electromagnetic scattering from a finitely-sized dielectric structure that is illuminated by an incoming field. This type of problem includes electromagnetic band gap materials and other metamaterials [1] that can be built using dielectric objects, dielectric diffractive optics [2] such as dielectric binary diffractive lenses [3], and photonic integrated circuits [4, 5] such as grating couplers and polarization converters.

Many numerical methods (solvers) that have been developed can solve this type of problem. In general, a trade-off between flexibility and speed of a numerical method is made. A class of solvers that does not exploit symmetries includes local methods, such as finite difference time domain (FDTD) [6], finite element method (FEM) [7], and finite integration technique (FIT) [8]. The flexibility of these methods has led to a widespread use of these approaches in commercial software.

Here, we are interested in the scattering from a dielectric object of finite size in a homogeneous background medium. We choose to employ a global method; an integral equation approach. With this approach it is possible to exploit the translation symmetry of the homogeneous background medium. Because of this symmetry, the Green function is a function of only the distance between source and observer. As a consequence, the spatial-domain convolution between the contrast current density and the Green function can be performed in the spectral domain, where it is simply a pointwise multiplication. This pointwise multiplication can in principle be performed much faster than a convolution and therefore it can lead to an efficient algorithm.

Historically, the Conjugate Gradient Fast Fourier Transform (CGFFT) [9] pioneered the exploitation of a spectral representation for a fast convolution. Even though CGFFT is a spatial method, with the use of FFTs the convolution is performed in a discrete spectral domain, which is fast. Improvements on this method are the Adaptive Integral Method (AIM) [10] and pre-corrected FFT (pFFT) [11], which use a meshing to accurately describe the scatterer and a grid of multipoles that

---

*Received 14 June 2016, Accepted 3 September 2016, Scheduled 18 September 2016*

\* Corresponding author: Roeland J. Ditz (r.ditz@tue.nl).

The authors are with the Eindhoven University of Technology, The Netherlands.

approximate the radiation from the mesh at a large distance. On this grid FFTs can be used again for efficiency.

The translation symmetry can also be exploited by using a spectral discretization of the problem. Although we are interested in aperiodic problems, it is fascinating to see that for periodic problems several algorithms exist that are based on a spectral representation. A key ingredient is that periodicity inherently leads to a discrete set of modes as a basis for the spectral domain. This is exploited in Rigorous Coupled Wave Analysis (RCWA) [12, 13], the C-method [14, 15] and the Periodic Volume Integral Method (PVIM) [16].

Based on these periodic solvers it is possible to calculate the scattering by aperiodic scatterers as well. For example, by using Perfectly Matched Layers (PMLs), where a scatterer of finite size is placed inside a box with absorbing sides that can be periodically repeated and solved with a periodic solver [17]. However, we are looking for a method that applies a discretization directly in the spectral domain.

Inspired by the success of CGFFT, AIM and pFFT, we understand the need for some sort of equidistant grid in the discretization. To achieve more flexibility, we intend to build an algorithm similar to meshless methods, so our discretization should be continuous in the spatial domain as well. Also inspired by the success of the aforementioned periodic spectral methods, we would like to use a spectral discretization. The method should work for aperiodic scatterers, so we need to find a discretization that is continuous in the spectral domain as well.

A discretization with a Gabor frame [18–20] fits these requirements. We explicitly choose the Gabor frame over the Gabor basis, because within the Gabor frame the convergence of the discretization is much better than the Gabor basis, where the convergence is hindered by the Balian Low theorem [21, 22]. The Gabor frame consists of a set of window functions defined on a uniform grid that are modulated by a set of equidistant frequencies. By a Fourier transform, the spatial Gabor frame yields a spectral Gabor frame as well. Because the Gabor frame employs window functions, it has the advantage of being localized spatially as well as spectrally. Moreover, a transformation from the spatial to the spectral domain is almost trivial. Because there is a discrete translation symmetry in the equidistant window functions, several fast methods exist to perform calculations on functions represented by a Gabor frame based on the FFT [19, 20, 23].

The Gabor frame has been used before to solve diffraction problems by line or surface scatterers as a source for Gaussian Beams [24–27]. These articles show that this method can be very useful for efficient calculation of the scattered field at a large distance (in terms of wavelengths), owing to an efficient long-distance approximation. However, to solve a domain integral equation we need to calculate the field at short distances as well, so this approximation is not beneficial. Related to the Gabor frame is the Wilson basis [28]. There are some reports on using the Wilson basis [29] as a discretization for electric fields or to solve a problem using projection methods [30], but none of them mention an optimized numerical structure that uses this type of basis and testing functions. Optimization is vital for this method to become competitive compared to other numerical methods in the sense of calculation time.

Here we show a first version of an algorithm that uses the Gabor frame in a domain integral equation. We use the Gabor frame in only one direction of the two-dimensional transverse-electric (TE) scattering problem and use a spatial discretization in the other direction just as in [16]. This also allows us to compare the accuracy for both discretizations.

## 2. THE DOMAIN INTEGRAL EQUATION

### 2.1. Problem Formulation

Consider a dielectric object described by a permittivity function in the  $x$ - $z$  plane, i.e.,  $\varepsilon_r(x, z)$ , illuminated by an incident electromagnetic field with the electric field polarized in the  $y$  direction, i.e., TE polarization. The permittivity function is different from 1 in the region bounded by  $x \in [-W, W]$ ,  $z \in [0, H]$  and we define the contrast function,

$$\chi(x, z) = \varepsilon_r(x, z) - 1, \quad (1)$$

where the background medium is vacuum. Owing to the two-dimensional configuration and the polarization of the electric field, the total electric field has only a  $y$ -component,  $\mathbf{E}(x, z) = E(x, z)\hat{\mathbf{y}}$ .

The scattering setup is shown in Fig. 1.

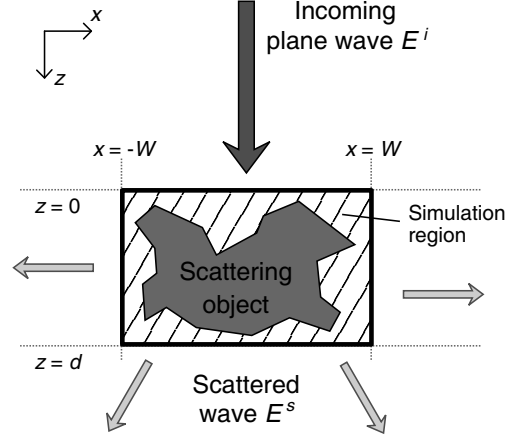


**Figure 1.** The 2D scattering problem.

We define the contrast current density by the relation  $J = j\omega\varepsilon_0\chi E$  and will make the distinction between the incoming field  $E^i$ , the scattered field  $E^s$  and the contrast current densities  $J^i$  and  $J^s$  they induce in the dielectric scatterer

$$\begin{aligned} E(x, z) &= E^i(x, z) + E^s(x, z), \\ J^{i/s}(x, z) &= j\omega\varepsilon_0\chi(x, z)E^{i/s}(x, z). \end{aligned} \quad (2)$$

The Fourier transform in the  $x$  direction is defined by

$$\hat{\varphi}(k_x) = \mathcal{F}_x[\varphi(x)](k_x) = \int_{-\infty}^{\infty} dx \varphi(x) e^{-jk_x x}, \quad (3)$$

and its inverse

$$\varphi(x) = \mathcal{F}_{k_x}^{-1}[\hat{\varphi}(k_x)](x) = \frac{1}{2\pi} \int_{-\infty}^{\infty} dk_x \hat{\varphi}(k_x) e^{jk_x x}. \quad (4)$$

We will use  $k_x$  as a variable for all spectral functions and  $x$  as a variable for spatial functions, dropping the hat for convenience.

## 2.2. The Integral Form of the 2D TE Scattering Problem

The Maxwell equations [31], assuming time convention  $e^{j\omega t}$ , are given by

$$\begin{aligned} \nabla \times \mathbf{H} &= j\omega \mathbf{D} \\ \nabla \times \mathbf{E} &= -j\omega \mathbf{B}. \end{aligned} \quad (5)$$

In a dielectric material we have  $\mathbf{B} = \mu_0 \mathbf{H}$  and  $\mathbf{D} = \varepsilon_0(1 + \chi)\mathbf{E}$ . The spectral domain Green function for the 2D transverse electric problem can be written as

$$G(k_x, z|z') = \frac{e^{-\gamma|z'-z|}}{2\gamma}, \quad (6)$$

where  $\gamma^2 = k_x^2 - k_0^2$  and  $k_0^2 = \omega^2 \varepsilon_0 \mu_0$ .

We can express the scattered field by the integral representation

$$E^s(k_x, z) = \frac{1}{j\omega\varepsilon_0} \int_0^d dz' G(k_x, z|z') k_0^2 J(k_x, z'), \quad (7)$$

which together with Eq. (2) can be written as

$$\begin{aligned} & -k_0^2 \chi(x, z) \mathcal{F}_{k_x}^{-1} \left[ \int_0^d dz' G(k_x, z|z') J^i(k_x, z) \right] (x) \\ & = J^s(x, z) + k_0^2 \chi(x, z) \mathcal{F}_{k_x}^{-1} \left[ \int_0^d dz' G(k_x, z|z') J^s(k_x, z) \right] (x), \end{aligned} \quad (8)$$

with the advantage that the contrast current density  $J$  is compactly supported, since the contrast  $\chi$  has a finite support. Now the left-hand side depends on the known incident field  $E^i(k_x, z)$  and the right-hand side can be viewed as an operator working on the scattered current, which we want to calculate. With the Fourier transforms we emphasize that we want to do the convolution in the  $x$ -direction in the spectral domain. In the  $z$  direction the convolution is done spatially.

### 2.3. Discretization along the $z$ Direction

Along the  $z$  direction we will use piecewise-linear functions  $\Lambda_n$  as expansion functions. These expansion functions are given by

$$\Lambda_n(z) = \begin{cases} 1 - \frac{|z-n\Delta|}{\Delta} & \text{if } |z - n\Delta| < \Delta \\ 0 & \text{if } |z - n\Delta| > \Delta \end{cases}, \quad (9)$$

with  $\Delta$  the stepsize in the  $z$  discretization. This discretization is convenient, because the electric field is continuous, and the contrast density is continuous in regions where  $\chi$  is continuous. When the contrast current density  $J(k_x, z)$  is expanded into the expansion functions, we obtain

$$J(k_x, z) \approx \sum_{n=0}^{N_z} J_n(k_x) \Lambda_n(z), \quad (10)$$

where  $N_z$  is the total number of expansion functions in the  $z$  direction. We use Dirac-delta testing functions in the  $z$  direction to find the coefficients  $J_n(k_x)$ , since it was observed that this leads to a well-conditioned linear system for a similar formulation for periodic scattering problems [16].

Now we have set up the sets of testing and expansion functions, they will be used on the integral equation Eq. (6). Because the Green function is semi-separable in  $z$ , it is advantageous to write

$$\begin{aligned} E_n^s(k_x) &= \int_0^{n\Delta} dz' \sum_{n'=0}^{n+1} G(k_x, n\Delta|z') k_0^2 J_{n'}(k_x) \Lambda_{n'}(z') + \int_{n\Delta}^d dz' \sum_{n'=n-1}^{N_z} G(k_x, n\Delta|z') k_0^2 J_{n'}(k_x) \Lambda_{n'}(z') \\ &= K_n^u(k_x) + K_n^d(k_x). \end{aligned}$$

Here the integral is splitted along  $z'$  in the two integrals  $K_n^u(k_x)$  and  $K_n^d(k_x)$ . There exists a recursive algorithm to find these two integrals using the fact that  $J_n(k_x)$  is nonzero only on the support of the contrast source. We will only perform the calculation for  $K_n^u$ , since  $K_n^d$  is similar. Working this out we find

$$\begin{aligned} K_{n+1}^u(k_x) &= K_n^u(k_x) e^{-\gamma\Delta} - J_n(k_x) \int_0^\Delta dz' k_0^2 \Lambda_0(z') \frac{e^{-\gamma(\Delta-z')}}{2\gamma} - J_{n+1}(k_x) \int_0^\Delta dz' k_0^2 \Lambda_1(z') \frac{e^{-\gamma(\Delta-z')}}{2\gamma} \\ &= K_n^u(k_x) e^{-\gamma\Delta} + J_n(k_x) I_m^u(k_x) + J_{n+1}(k_x) I_e^u(k_x), \end{aligned} \quad (11)$$

where  $I_m^u$  and  $I_e^u$  are introduced for the result of the integrals over  $z'$ . With this method we can calculate  $K_n^{u/d}(k_x)$  for all  $n$  in only  $N_z$  steps. This yields an algorithm of linear complexity in  $N_z$ .

### 2.4. Far-Field Intensity

In the end we are interested in the far field due to the contrast source. Since the electric field at a large distance is needed, we use a different method than in the previous section to calculate this.

We start again from the integral representation in Eq. (7). Using the discretization in the  $z$  direction this is written as

$$E^s(k_x, z) = \frac{j}{\omega \varepsilon_0} \int_{-\Delta}^{\Delta} dz' \sum_{n=0}^{N_z} k_0^2 J_n(k_x) \frac{e^{-j\sqrt{k_0^2 - k_x^2}|n\Delta + z' - z|}}{2\sqrt{k_0^2 - k_x^2}} \Lambda(z'). \quad (12)$$

By taking the inverse Fourier transformation in the  $x$  direction and by changing to polar coordinates  $x = R \cos \varphi$ ,  $z = R \sin \varphi > 0$  in the limit  $R \rightarrow \infty$ , we obtain

$$E^s(R, \varphi) = \frac{j}{2\omega \varepsilon} \sum_{n=0}^{N_z} k_0^2 J_n(-\cos \varphi) e^{jk_0 n \Delta \sin \varphi} \frac{2 - 2 \cos(\Delta \sin \varphi)}{\Delta \sin^2 \varphi} (J_0(R) + jH_0(R)),$$

with  $J_0$  the Bessel function of the first kind of order zero and  $H_0$  the Struve function of order zero.

The field strength depends on the distance and owing to energy conservation the field strength will decay as  $1/\sqrt{R}$ . Therefore, we will employ the scattering strength  $S(\varphi)$  as a function of the angle  $\varphi$ , defined as

$$S(\varphi) = \lim_{R \rightarrow \infty} R |E^s(R, \varphi)|^2. \quad (13)$$

### 3. DISCRETIZATION IN THE X DIRECTION VIA A GABOR FRAME

To discretize Eq. (8) in the  $x$ -direction we will employ a Gabor frame. We begin with a short description of the way we have implemented the Gabor frame. Then we list the mathematical operations needed to apply on functions represented using a Gabor frame and explain their implementation. We end by discussing the uniqueness of the numerical solution.

#### 3.1. Definition

Following the exposition in [20] to introduce the Gabor frame and its properties, we show how we have implemented the Gabor frame. A Gabor transform makes extensive use of a window function  $g(x)$ , for which we choose here the Gaussian

$$g(x) = 2^{\frac{1}{4}} e^{\left(-\pi \frac{x^2}{X^2}\right)}, \quad (14)$$

with  $X$  the parameter that defines the width of the window function. The Gabor frame is defined by

$$g_{mn}(x) = g(x - m\alpha X) e^{jn\beta Kx}, \quad (15)$$

with the modulation step size  $K$ , defined by  $KX = 2\pi$ , and  $\alpha$  and  $\beta$  two constants defining the oversampling, obeying  $\alpha\beta \leq 1$ . Function values of a function  $f(x)$  that is represented by Gabor coefficients  $f_{mn}$  can be calculated by

$$f(x) = \sum_{m=-\infty}^{\infty} \sum_{n=-\infty}^{\infty} f_{mn} g_{mn}(x) = \sum_{m,n} f_{mn} g_{mn}(x). \quad (16)$$

Here the  $m$  sum is over spatial windows, and the  $n$  sum is over the modulation frequencies. In practice these sums are truncated. To calculate the coefficients  $f_{mn}$  of a given function  $f(x)$  it is common to write

$$f_{mn} = \int_{-\infty}^{\infty} dx f(x) \gamma_{mn}^*(x), \quad (17)$$

where we introduced the dual window function  $\gamma(x)$  that forms the dual frame to  $g_{mn}(x)$ . Here  $*$  denotes complex conjugation. The indices have a meaning similar to Eq. (15), i.e.,

$$\gamma_{mn}(x) = \gamma(x - m\alpha X) e^{jn\beta Kx}. \quad (18)$$

Several methods to calculate a dual window function  $\gamma(x)$  are described in [19, 20].

### 3.2. The Choice for the Gabor Frame

From Eq. (17) it is clear that the dual window function  $\gamma(x)$  is very important to achieve an efficient representation of a function. The Balian Low theorem states that a good dual window only exists when oversampling is employed ( $\alpha\beta < 1$  in Eq. (17)) [21, 22]. The dual window of an oversampled Gabor frame can be chosen in a way that it converges exponentially both spatially and spectrally [19, 20, 23]. We use the dual window obtained through the Moore-Penrose inverse, since it is the one most commonly used and it exhibits good convergence.

After the construction of a dual window, it is possible to calculate the Gabor coefficients of functions by Eq. (17). There are faster ways to calculate Gabor coefficients for rational oversampling  $\alpha\beta = q/p$  with  $p > q \in \mathbb{N}$ . In that case it is possible to use FFTs in  $O(pn \log n)$  operations, with  $n$  the total number of Gabor coefficients [19, 23]. This method is faster, but it uses an equidistant sampling on the function from which it calculates the Gabor coefficients, so it only works well for sufficiently smooth functions.

When functions have discontinuities, we should evaluate the integrals in Eq. (17), but we found that this is a very slow method. Another option is to approximate this result by using oversampling in the FFT method to calculate the coefficients  $f_{mn}$  of  $f(x)$  for a broader range of  $n$  and later discard the extra coefficients. When more modulation frequencies are used, the function is sampled on a finer lattice and therefore the approximation error is smaller.

### 3.3. Building Blocks

To solve an integral equation using the method outlined in Section 2.2, we need methods to manipulate functions represented by Gabor coefficients. It is of course important that these algorithms scale well,  $O(N \log N)$  or better, where  $N$  denotes the number of Gabor coefficients.

From Eq. (11) and Eq. (2) we see that the following operations on Gabor coefficients are required

- Addition.
- Multiplication by a scalar.
- Fourier transform and inverse Fourier transform.
- Multiplication by a set of Gabor coefficients.
- Convolution with a set of Gabor coefficients.
- Inner product.

The first two operations are trivial and can be performed per coefficient. The convolution can be calculated using a combination of a Fourier transform, a spectral multiplication and an inverse Fourier transform. In the following we explain how to calculate the Fourier transform, the multiplication, and inner product on sets of Gabor coefficients.

### 3.4. Fourier Transform

A very convenient property of the Gabor frame functions is that their Fourier transform also yields a Gabor frame. We define a spectral frame function  $\hat{g}_{nm}(k)$  by

$$\hat{g}_{nm}(k) = \mathcal{F}_x[g_{mn}(x)](k) = \hat{g}(k - n\beta K) e^{jm\alpha X k} e^{2\pi j\alpha\beta mn}, \quad (19)$$

with the spectral window function  $\hat{g}(k) = \mathcal{F}_x[g(x)](k)$ .

On the level of Gabor coefficients, the Fourier transform  $\hat{f}(k)$  of the function  $f(x)$  can be represented by

$$\hat{f}(k) = \sum_{m,n} \hat{f}_{mn} \hat{g}_{mn}(k), \quad (20)$$

where

$$\hat{f}_{mn} = f_{nm} e^{-2\pi j\alpha\beta mn}. \quad (21)$$

With this definition of a spectral Gabor frame, the operation of Fourier transformation is computationally very easy and can be done in  $O(N)$  steps, where  $N$  is the total number of Gabor

coefficients. Of course it would have been possible to use a different Gabor frame for the spectral representation, but this one has the advantage that a Fourier transform can be obtained from the simple relation Eq. (21). When the spectral frame is not simply the Fourier transform of the spatial frame, such a simple relationship does not exist.

### 3.5. Multiplication of Two Sets of Gabor Coefficients

Although there exists an easy and very fast way to calculate a Fourier transform of a function, with Gabor coefficients it is the multiplication of functions that takes most of the time. When we multiply function  $v(x)$  and  $w(x)$  their product,  $f(x)$  can be written as

$$f(x) = v(x)w(x) = \sum_{m,n} \sum_{k,l} v_{mn} w_{kl} g_{mn}(x) g_{kl}(x). \quad (22)$$

When we define the functions  $A_j(x) = g(x)g(x - j\alpha X)$ , their Gabor coefficients  $A_{j;pq}$  are useful for the calculation of the product

$$g_{mn}(x)g_{kl}(x) = \sum_{r,s} A_{k-m;r-m,s-n-l} g_{rs}(x) e^{2\pi j\alpha\beta m(n+l-s)}.$$

Now we would like to calculate the Gabor coefficients  $f_{mn}$  of  $f(x)$  directly from  $v_{mn}$  and  $w_{mn}$ . We can use  $A_{j;pq}$  in Eq. (22) to obtain

$$f(x) = \sum_{r,s} \sum_{m,n} \sum_{k,l} A_{k-m;r-m,s-n-l} v_{mn} w_{kl} g_{rs}(x) e^{2\pi j\alpha\beta m(n+l-s)}. \quad (23)$$

After two variable substitutions,  $a = n + l$  and  $b = k - m$

$$f_{rs} = \sum_{b=-B}^B \sum_{m,a} T_{b;m,a} A_{b;r-m,s-a} e^{2\pi j\alpha\beta m(a-s)} \quad (24)$$

is obtained, with

$$T_{b;m,a} = \sum_n v_{mn} w_{m+b,a-n}, \quad (25)$$

and  $B$  defining the truncation number in the  $b$  summation. The  $T_{b;m,a}$  can be calculated efficiently using FFTs, because they are calculated from a discrete convolution in  $n$ .  $B$  does not need to be large, because  $A_b(x)$  decays quickly when the overlap between the window functions is small. For example with  $\alpha = \beta = \sqrt{2/3}$  oversampling and the window function as in Eq. (14) we find  $|A_{\pm 3}(x)|_{\mathcal{L}^2} < 10^{-5} |A_0(x)|_{\mathcal{L}^2}$ . In our case a sum of 5 terms ( $B = 2$ ) would already be enough for an accuracy much better than  $10^{-4}$  in this sum. So  $T$  is only needed for a small number of  $b$  values. The number of significant  $m$  and  $a$  combinations is of the order  $N$ , the total number of coefficients of the input functions.

The exponential factor in Eq. (24) has only  $p$  different values for a  $q/p = \alpha\beta$  oversampled Gabor frame. We can exploit this, by carrying out the  $m$  summation for every different value of  $s \in \{1 \dots p\}$  individually. Then we can use that the  $m$  and  $a$  summation can be written as a convolution and therefore this summation can be done efficiently using FFTs as well. The total complexity scales like  $NpB \log N$ , with  $N$  the total number of Gabor coefficients.

### 3.6. Inner Products

The  $\mathcal{L}^2(\mathbb{R})$  inner product of functions  $f(x)$  and  $h(x)$  can in principle be calculated from

$$\langle f, h \rangle = \int_{-\infty}^{\infty} dx f(x) h^*(x) = \sum_{k,l,m,n} f_{kl} h_{mn}^* \int_{-\infty}^{\infty} dx g_{kl}(x) g_{mn}^*(x). \quad (26)$$

Because of the spectral and spatial translation symmetry, the inner product between the frame functions  $g_{mn}(x)$  and  $g_{kl}(x)$  can be further simplified to

$$\begin{aligned}\langle g_{kl}, g_{mn} \rangle &= \int_{-\infty}^{\infty} dx g(x - \alpha k X) g^*(x - \alpha m X) e^{j(l-n)\beta K x} \\ &= e^{2\pi j \alpha \beta k(l-n)} \int_{-\infty}^{\infty} dx g(x) g^*(x - \alpha(m-k)X) e^{i(l-n)\beta K x} \\ &= e^{2\pi j \alpha \beta k(l-n)} \mathcal{M}_{k-m, l-n},\end{aligned}\tag{27}$$

so it can be used to calculate the inner product

$$\langle f, h \rangle = \sum_{k,l,m,n} f_{kl} h_{mn}^* e^{2\pi j \alpha \beta k(l-n)} \mathcal{M}_{k-m, l-n}.\tag{28}$$

Here we see the same exponential  $e^{2\pi j \alpha \beta k(l-n)}$  as for the multiplication. Because of the rational oversampling there are only  $p$  unique sequences for the exponential as a function of  $(l-n)$ . Now the discrete convolution of  $h_{mn}$ , with  $e^{2\pi j \alpha \beta k(l-n)} \mathcal{M}_{k-m, l-n}$ , can be done using FFTs again for each of these  $p$  unique discrete convolution kernels.

The methods described in the previous subsections are exact, except for the multiplication and inner products of coefficients, which converge exponentially with the number of terms included.

### 3.7. The Discrete Formulation

By discretizing Eq. (8) as described at the end of Section 2.2, our problem can be written as

$$A \circ J^s = -(1 + A) \circ J^i,\tag{29}$$

with

$$J^{i/s}(k_x, z) = \sum_{m=-M}^M \sum_{n=-N}^N \sum_{\ell=0}^{N_z} J_{mn, \ell}^{i/s} g_{mn}(k_x) \Lambda_p(z).$$

The operation  $A \circ$  then represents the Green function  $G$  convolution and contrast  $\chi$  multiplication and an addition of  $J$ , as in the right-hand side of Eq. (8).

When we view  $J^s$  and  $A \circ J^i$  as lists of numbers, then the operator  $A$  can be viewed as a matrix and we can write  $\underline{\underline{A}} \cdot \underline{j} = \underline{b}$ .

Normally one would continue by inverting this matrix, but this matrix is not invertible because of the oversampling in the Gabor frame. It is for example possible to write a function that is zero everywhere, with non-vanishing coefficients; in other words the Gabor-frame representation has a nontrivial null-space. However, since we make a fixed choice for a certain dual window  $\gamma$  (see Section 3.1), the representation of every function in the Gabor frame becomes unique. We used GMres to solve the overall linear system.

## 4. SINGULAR BEHAVIOUR OF THE GREEN FUNCTION

When we calculate the Gabor coefficients of  $K_n^{u/d}(k_x)$  for every  $n$  recursively according to Eq. (11), there can be severe discontinuities in the derivative of  $K_n^{u/d}(k_x)$  around  $k_x = \pm k_0$ . The main reason is the first term in Eq. (11)

$$K^u(k_x, z) = K^u(k_x, z - \Delta) e^{-\gamma \Delta} + \dots = K^u(k_x, 0) e^{-n \Delta \gamma} + \dots,\tag{30}$$

with  $z = n\Delta$  the height where we would like to evaluate the field. In the present discussion we ignore everything related to current density.

In Fig. 2(a) we show a spectral representation of an electric field due to a point source. In Fig. 2(b) we show the field of this point source propagated one  $\Delta$  step in the  $z$  direction. The discontinuous derivative is clearly visible, but does not look severe. After propagating further in the  $z$ -direction (Fig. 2(c)), the discontinuity in the derivative becomes more severe. After several wavelengths of  $z$

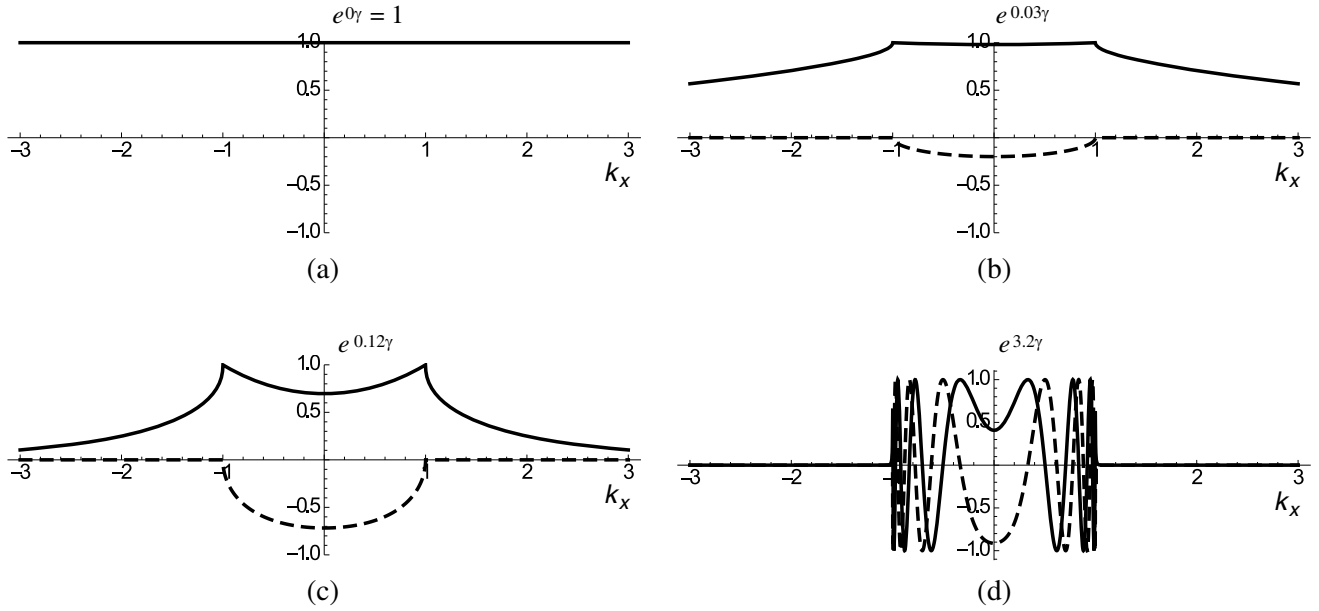


**Figure 2.** The spectrum (real part: solid, imaginary part: dashed) of a wave ( $k_0 = 2\pi/\lambda$ ) emanating from a point source at  $z = 0$ . In (a) through (d) we subsequently plotted the spectrum at  $z = 0$ ,  $z = 0.03\lambda$ ,  $z = 0.12\lambda$ ,  $z = 3.2\lambda$ . It can be clearly seen how the smoothness deteriorates for large  $z$  near  $k_x = \pm k_0$ .

propagation, oscillations start to appear in  $K^u(k_x, z)$  for  $k_x$  between  $-k_0$  and  $k_0$  in Eq. (30), as is shown in Fig. 2(d).

The strong discontinuity of its derivative makes it hard to represent this function by Gabor coefficients, because a finite set of Gabor coefficients is limited in its spectral representation. It is important to note that although the function  $e^{-\gamma z}$  is highly oscillatory for large  $z$ , its inverse Fourier transform  $\mathcal{F}_{k_x}^{-1}[e^{-\gamma z}](x)$  is continuous, but extends to large distances in  $x$ . This implies that it should still be possible to find a good representation by Gabor coefficients that holds only in the simulation domain  $x \in [-W, W]$ . Intuitively, one would truncate the number of spatial Gabor coefficients. However, it is inaccurate to multiply spatially-truncated representations of  $e^{-\gamma \Delta}$ , as would be done in the recursive algorithm Eq. (11). The error results from the fact that a spectral multiplication corresponds to a spatial convolution. Spatially (the inverse Fourier transform of)  $e^{-\gamma \Delta}$  does not have a bounded support. For a convolution of two functions with infinite spatial support, information about the entire support of these functions is needed. For this reason we would need the Gabor coefficients to represent the function over the entire  $x$ -axis, which takes an infinite number of coefficients.

A more convenient method is to use a coordinate scaling in the spectral domain. The goal of the scaling is to allow for an accurate and efficient representation of the field  $K_n^{u/d}(k_x)$ . In principle there are many choices for a scaling function that would work, but there is also a  $1/\gamma$  singularity in the Green function Eq. (6). We will incorporate the  $1/\gamma$  singularity in the Jacobian of the scaling, so it will be cancelled. Scaling a function that is represented using Gabor coefficients is not a trivial task, since it is part of the core of the algorithm, and it needs to result in fast calculations.

#### 4.1. The Scaled Coordinates

Figure 3(b) shows an example for an unscaled  $e^{-\gamma H}/\gamma$ . The many oscillations and the two asymptotes make it difficult to represent this function using a Gabor frame. We want to make a good approximation of the Green function of waves generated at  $z = 0$  that propagate all the way to the  $z = H$ , which is the largest distance and therefore the worst case. We make use of three scaling functions  $s_1$ ,  $s_2$  and  $s_3$ , which will be optimized for different parts of the spectral domain. From this set of functions one

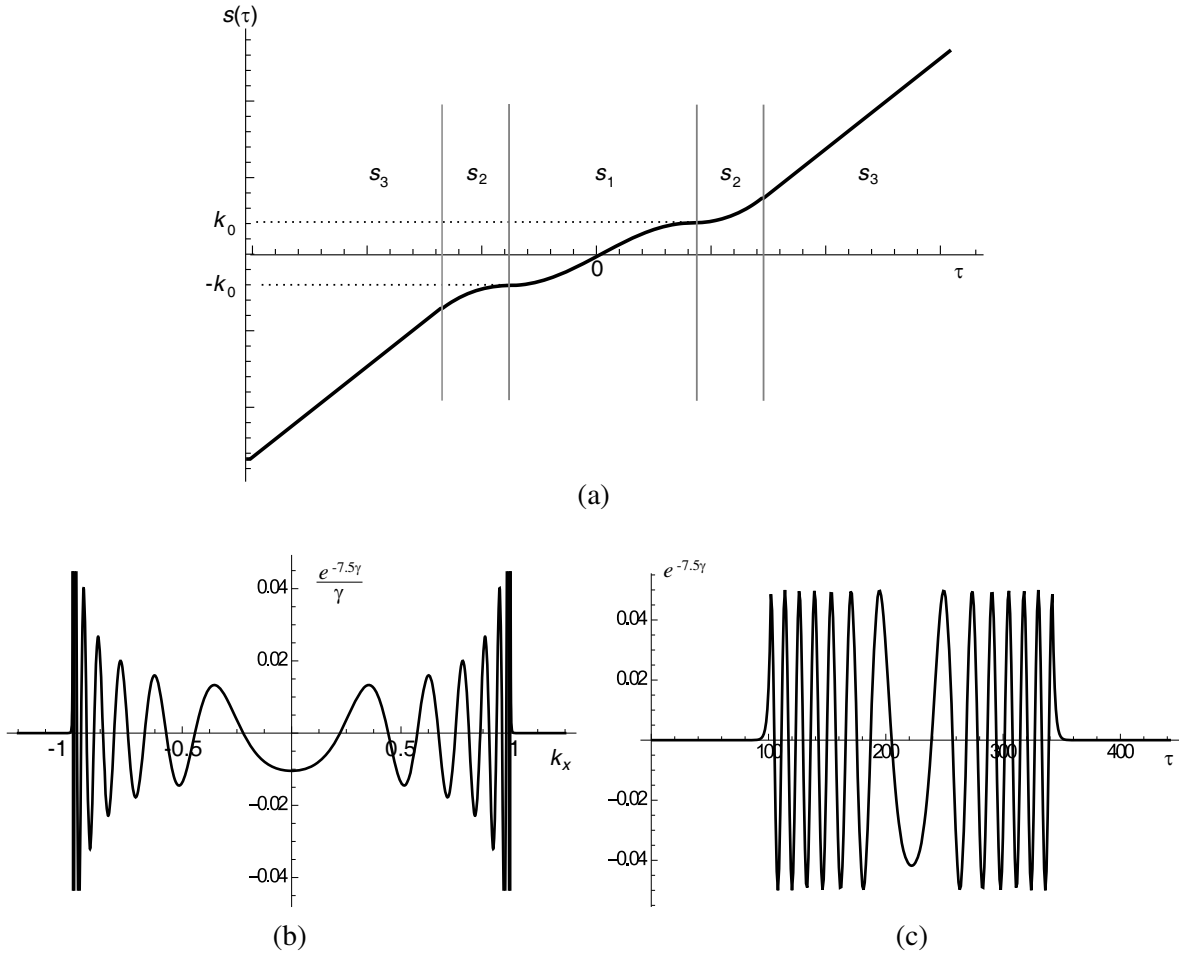


**Figure 3.** (a) A typical scaling function. (b) The unscaled  $e^{-7.5\gamma}/\gamma$ . (c) The scaled  $e^{-7.5\gamma}$  (the factor  $1/\gamma$  disappears with the Jacobian).

scaling function  $s$  will be composed, which uses the most appropriate scaling function for every part of the  $k_x$  axis.

We choose the first part of the scaling function for  $|k_x| < k_0$  such that the  $\frac{1}{\gamma}$  factor is incorporated in the Jacobian of the scaling by using a sine transformation

$$k_x(\tau) = s_1(\tau) = k_0 \sin(c\pi\tau/2). \quad (31)$$

The second part of the scaling function works just outside that region, for  $|k_x| > k_0$ , and it can be seen as a continuation of the scaling function  $s_1$

$$s_2(\tau) = \begin{cases} k_0 \cosh(c\pi(\tau - 1)/2) & \text{if } \tau > 1/c \\ -k_0 \cosh(c\pi(\tau + 1)/2) & \text{if } \tau < -1/c. \end{cases} \quad (32)$$

These scaling functions  $s_1$  and  $s_2$  will also smoothen the oscillations in  $e^{-\gamma H}$  when the constant  $c$  is chosen small enough, depending on  $H$  and  $k_0$ . To decide on a value for  $c$  the  $1/\gamma$  derivative is most important when  $H$  is small. When the simulation height  $H$  gets larger  $e^{-\gamma H}$  becomes the governing factor to determine  $c$ . A simple plot of  $e^{-\gamma H}$  as in Fig. 3(c) can show whether or not the choice for the constant  $c$  is good; it should show a well sampled continuous curve.

The third part of the scaling function has the constraint that the derivative of the scaling function should never exceed one. Otherwise information from the input function is lost due to a coarser sampling in the scaled coordinates. It is defined by

$$s_3(\tau) = \tau + d, \quad (33)$$

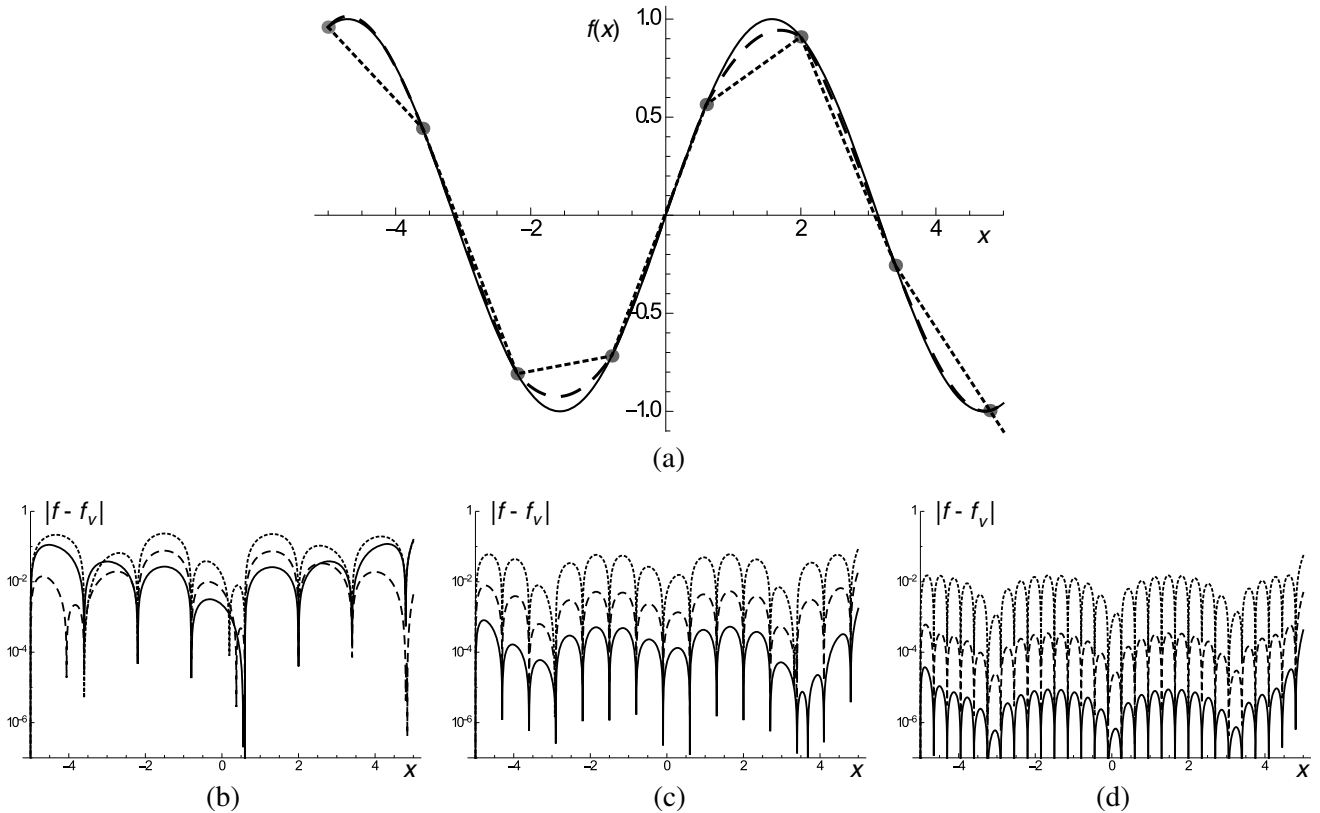


**Figure 4.** (a) Solid line:  $f_V(x)$  a sine function as validation. Dotted: A linear interpolation  $f$  of the validation  $f_V$ , dashed: A third order Hermite spline interpolation  $f$  of the validation  $f_V$ . (b) The absolute error of the approximations  $|f(x) - f_V(x)|$ : linear interpolation (dotted), 3rd order Hermite interpolation (dashed), 5th order Hermite interpolation (solid). (c) The same for double sampling. (d) The same for quadruple sampling.

with  $d$  a constant that allows to shift this function to make the transition to the other scaling functions smooth. In Fig. 3(a) we show how to put these functions together: The scaling function is put together such that for every  $k_x = s(\tau)$  the scaling function with the smallest derivative is used, and that transitions between the three scaling functions are smooth. For large values of  $c$  (small  $H$ ) another region with scaling function  $s_3$  in the middle is possible.

With this scaling an efficient representation of the electric field over the complete  $x$  axis with a limited number of  $k_x$  functions is made. Around the points  $k_x = \pm k_0$  we have already compensated the  $1/\gamma$  singularity in the Jacobian. This has the advantage that we do not have to worry about asymptotes, since the function is bounded now. For the region with scaling function  $s_3$  we still need to incorporate the  $1/\gamma$ , but it is well behaved there.

## 4.2. Interpolating to and from the Scaled Coordinates

### 4.2.1. From Equidistant to Scaled

With the algorithm from [19] we can go from a spectral-domain current with equidistant  $k_x$  sampling,  $J_n(k_m) = J_n(m\Delta_k)$  with  $m \in \mathbb{Z}$ , to Gabor coefficients  $J_{n;i,j}$  and back again. What we need is to have function values  $\tilde{J}_{n;m} = J_n(\tau_m)$  on the non-equidistant scaled coordinates  $\tau_m = s(m\Delta_k)$  as well with  $s(k_x)$  the scaling function. To obtain that, we need to interpolate the equidistant sampling in a smart manner, since linear interpolation leads to intolerably large errors. The tilde will denote functions on the scaled coordinates.

From Figs. 4(a) and (b) it is clear that the sampling rate is not high enough to get a good

approximation of the current density with the algorithm from [19] by using a high-order interpolation only. To get a better approximation we use oversampling: we pad the Gabor coefficients with zeroes for high  $|j|$  in  $J_{n,i,j}$  and then transform the Gabor coefficients to an equidistant sampling. In Figs. 4(c) and (d) it is shown that the combination of oversampling and a fifth order Hermite [32] interpolation reduces the error to a tolerable level.

#### 4.2.2. From Scaled to Equidistant

To go back from the scaled coordinates to equidistant coordinates, the total number of samples is reduced, especially around the singularities. We need to be careful not to throw away any important information in the process of resampling.

We transform directly from the scaled spectral coordinates to equidistant spatial coordinates on the interval  $x \in [-W, W]$ , since only spatially we are able to make a good approximation using a finite number of Gabor coefficients. Let us start from the inverse Fourier transform of the scaled-coordinate electric field

$$E_n(x_m) = \int_{-\infty}^{\infty} d\tau \mathcal{J}_s(\tau) \hat{E}_n(s(\tau)) e^{js(\tau)x_m} = \int_{-\infty}^{\infty} d\tau \tilde{E}_n(\tau) e^{js(\tau)x_m}, \quad (34)$$

with  $\mathcal{J}_s(\tau) = H_s(\tau)/\gamma$  with  $H_s(\tau)$  the Jacobian of the scaling function  $s$ , chosen to incorporate the  $1/\gamma$  factor from the Green function in Eq. (6). The  $x_m$  values are on an equidistant grid, such that this list can be used to transform to Gabor coefficients. The bounded function  $\tilde{E}_n(\tau) = \mathcal{J}_s(\tau)E_n(s(\tau))$  is defined by the list of function values on  $\tau_m$  through a linear interpolation

$$\tilde{E}_n(\tau) = \sum_m \Lambda_m(\tau) E_{n,m} \mathcal{J}_s(\tau), \quad (35)$$

with  $\Lambda$  the piecewise-linear function in Eq. (9), with  $\Delta = \Delta_k$  and  $E_{n,m} = E(s(m\Delta_k)) = E(\tau_m)$ , a list of function values as described in Section 4.2.1. The Jacobian is chosen in such a way so as to cancel the  $1/\gamma$  in the Green function Eq. (6). The linear interpolation is not ideal, but since we are downsampling, the error from this approximation is less of a problem than before, while upsampling.

Now we need to calculate the Fourier integral Eq. (34). Using an FFT would be desirable, but this is not possible because of the scaling. What we can do is approximate the integral in Eq. (34) by

$$E(x_m, z_n) \approx \frac{1}{2\pi} \sum_{n=-\infty}^{\infty} e^{jn\Delta_k x_m} \int_{(n-\frac{1}{2})\Delta_k}^{(n+\frac{1}{2})\Delta_k} dk \tilde{E}_n(s^{-1}(k)). \quad (36)$$

Here we recognize a discrete Fourier transform with sampling distance  $\Delta_k$  and function values given by the integral. The problem here is that we make the approximation

$$\int_{(l-\frac{1}{2})\Delta_k}^{(l+\frac{1}{2})\Delta_k} dk \tilde{E}_n(s^{-1}(k)) e^{jkx_m} \approx e^{jl\Delta_k x_m} \int_{(l-\frac{1}{2})\Delta_k}^{(l+\frac{1}{2})\Delta_k} dk \tilde{E}_n(s^{-1}(k)),$$

which only works for  $|x_m|$  small. When there are many samples in  $\tilde{E}_n(k)$  in the range of one  $\Delta_k$ -integral, and when  $|x_m|$  is larger, this approximation breaks down. Note that the scaling function has been chosen in such a way that the integral on the right-hand side is approximated very well. The problem is that we make a poor approximation when the complex exponential is put outside the integral.

When  $\tilde{E}_n(s^{-1}(k))$  is multiplied by  $e^{X_\ell k}$ , we should see a shift over  $X_\ell$  in its Fourier transform. Since we can calculate the Fourier transform of  $\tilde{E}_n(s^{-1}(k))$  accurately around  $x_m \approx 0$  (Eq. (36)), we can calculate the Fourier transform around  $X_\ell$  accurately as well by

$$E_{n;\ell}(x_m) \approx \frac{1}{2\pi} \sum_l e^{jn\Delta_k(x_m - X_\ell)} \int_{(l-\frac{1}{2})\Delta_k}^{(l+\frac{1}{2})\Delta_k} dk \tilde{E}_{n;\ell}(s^{-1}(k)) e^{jkX_\ell}, \quad (37)$$

which gives us approximations accurate around each  $X_\ell$  value. To calculate from this the electric field accurately at  $x_m$  a linear interpolation is employed. First we choose  $\ell$  such that  $X_\ell < x_m < X_{\ell+1}$ , then the field at  $x_m$  can be found by

$$E_n(x_m) = \frac{(x_m - X_\ell)E_{n;\ell}(x_m, z_n) + (X_{\ell+1} - x_m)E_{n;\ell+1}(x_m)}{X_{\ell+1} - X_\ell}. \quad (38)$$

**Table 1.** Specification of the validation cases.

Parameters	Circle	Rectangle	Grating
$\varepsilon_r$ of object	2	2	2
dimension of object (m)	$r = 1.35$	$2.0 \times 5.0$	five blocks, $1 \times 1.4$ , spacing 2
wavenumber $k_0$ ( $\text{m}^{-1}$ )	1.45	0.7388	1.5
angle of incidence $\theta$	$0^\circ$	$270^\circ$	$45^\circ$
validation	Analytic solution	JCMWave	None

We used this linear  $\ell$  interpolation with 9 different spatial sampling points  $x_0$ . This was enough to get a  $3 \cdot 10^{-3}$  relative error on a practical example of a contrast current. This will be enough for our purpose, but we can improve the accuracy by using higher order Hermite interpolations and by taking more  $X_\ell$  values.

It is important to remark here that the distance between the samples that make up  $\tilde{E}_n(\tau)$  is less than or equal to  $\Delta_k$ . This means that for the part that is scaled using  $s_3$ , the sampling is the same for the FFT. For the parts with  $s_1$  and  $s_2$  there is downsampling.

To summarize, our algorithm consists of the following steps:

- Start with a list of scaled spectral sampling of a function  $\tilde{E}_{n,m}$ .
- Interpolate using Eq. (35).
- Multiply the interpolation by exponentials  $E_{n;\ell}(\tau_m) = e^{jX_\ell s^{-1}(\tau_m)} E_n(\tau_m)$ .
- Integrate over the scaled interpolation function to obtain a list with (a coarser) equidistant sampling for every value of  $\ell$ . (the integral in Eq. (37)).
- Use an FFT on each  $\ell$ 's list to get results that are a good approximation around  $X_\ell$ .
- Interpolate between the result  $\ell$  and  $\ell + 1$  using Eq. (38).

### 4.3. Various Representations

Now to solve the integral equation Eq. (8), the challenge is to multiply by the contrast current in the spatial domain and multiply by the various parts of the Green function (e.g., Eq. (11)) in the spectral domain.

We start from a spatial representation of the electric field  $E_n(x)$ , spatial because it needs to be multiplied by the contrast function Eq. (1) to arrive at the current distribution  $J_n(x) = \chi_n(x)E_n(x)$ . The Gabor coefficients of  $\chi$  are calculated using the fast algorithm in [19] to approximate Eq. (17). Cutting off the highest spectral parts of the current distribution does not deteriorate the accuracy very much, so we might as well bound it spectrally. This means that Gabor coefficients are the most convenient representation for  $J_n(x)$ .

To calculate the convolution of the Green function with the current distribution we would like to use spectral domain in the  $x$  direction (see Eq. (11)). The choice of the scaled coordinates both compensates the divergent  $1/\gamma$  in the Green function, and it takes care of rapid oscillations in the Green function for large  $z$  propagation.

In Fig. 5 the flow of our algorithm through the various representations is represented.

## 5. RESULTS

We tested the accuracy of our algorithm on a circle, a rectangular scatterer and a small grating described in Table 1.

The incoming field is defined as  $E^i(x, z) = E_0 \exp(jk_0(x \cos \theta + z \sin \theta))$ , with  $E_0 = 1 \text{ V/m}$ . For the circle an analytical solution exists [33], which was used to validate our results. For the rectangle we used a numerical solution calculated using the JCMWave software package as a reference [34]. In the  $z$ -direction we choose  $\Delta = 0.05m$ . In the  $x$ -direction we used a Gabor frame with 13 ( $m \in \{-6, \dots, 6\}$ )

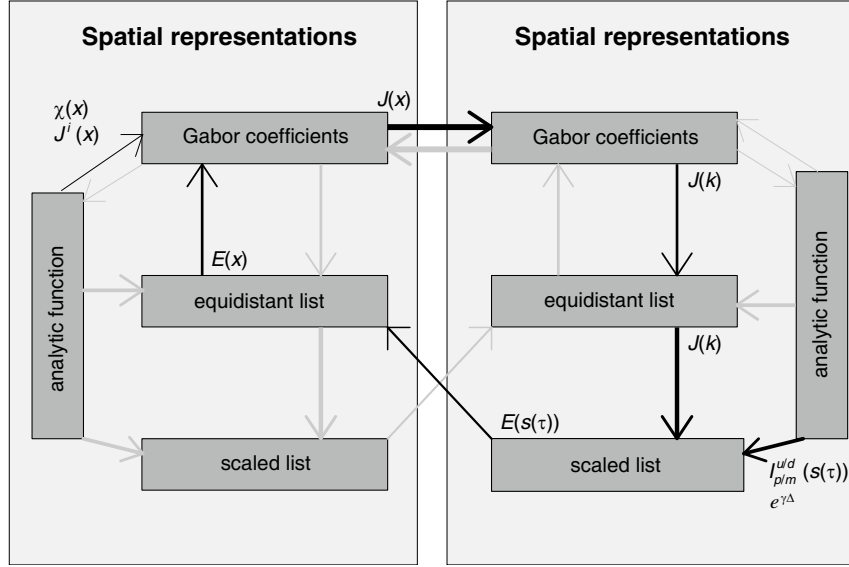


**Figure 5.** The various transformations and representations we have explained in Section 4. The thickness of the arrows signifies the speed of the transformation qualitatively. Thicker means faster. The black arrows signify the different transformations that are actually used in the algorithm, the grey ones are possible, but not used.

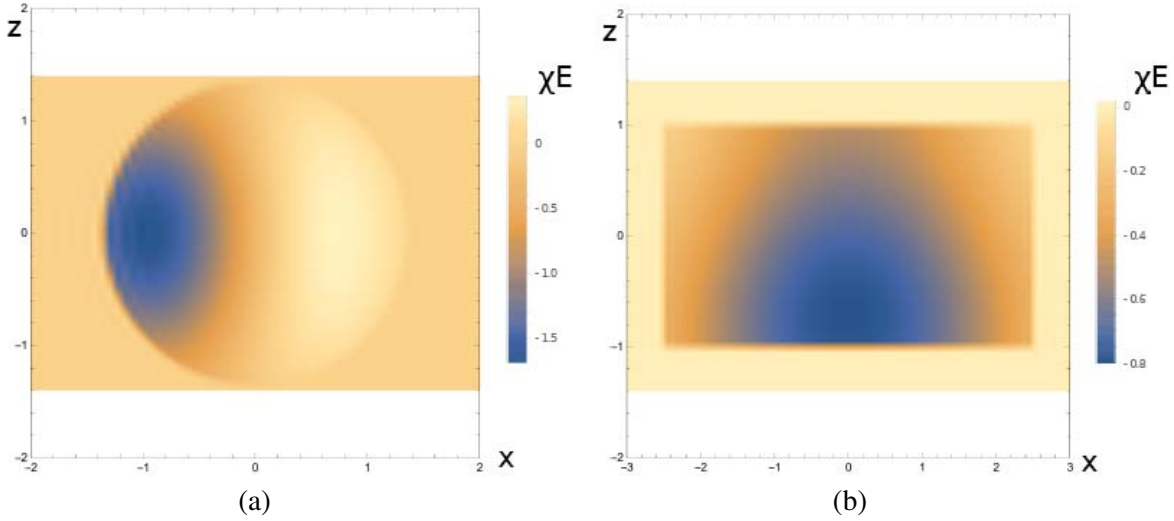


**Figure 6.** The real part of  $\chi E(x, z)$  (which is proportional to the contrast current), for (a) the circle and (b) the rectangle.

spatial windows and 7 ( $n \in \{-3, \dots, 3\}$ ) modulation frequencies (see Eq. (16)). The oversampling was at  $\alpha\beta = 3/2$  and  $X = 0.5m$  (see Eq. (15)). This means that per meter there are around 17 coefficients in the  $x$  direction and 20 in the  $z$  direction. We used  $16\ell$  values in going from scaled spectral sampling to the equidistant spatial sampling (see Section 4.2.2).

In Fig. 6 we show the real part of the simulation results for circle and the rectangle. Figs. 7(a), (b) show the absolute value of the difference between the electric field  $E$  from the validation results and  $\chi E$  from our simulations. It can be clearly seen that in the two different directions the approximation error has a different character, because we used a different discretization scheme. Especially for the circle it looks like the error is quite large, but this is mainly due to the Gibbs ringing around the discontinuity

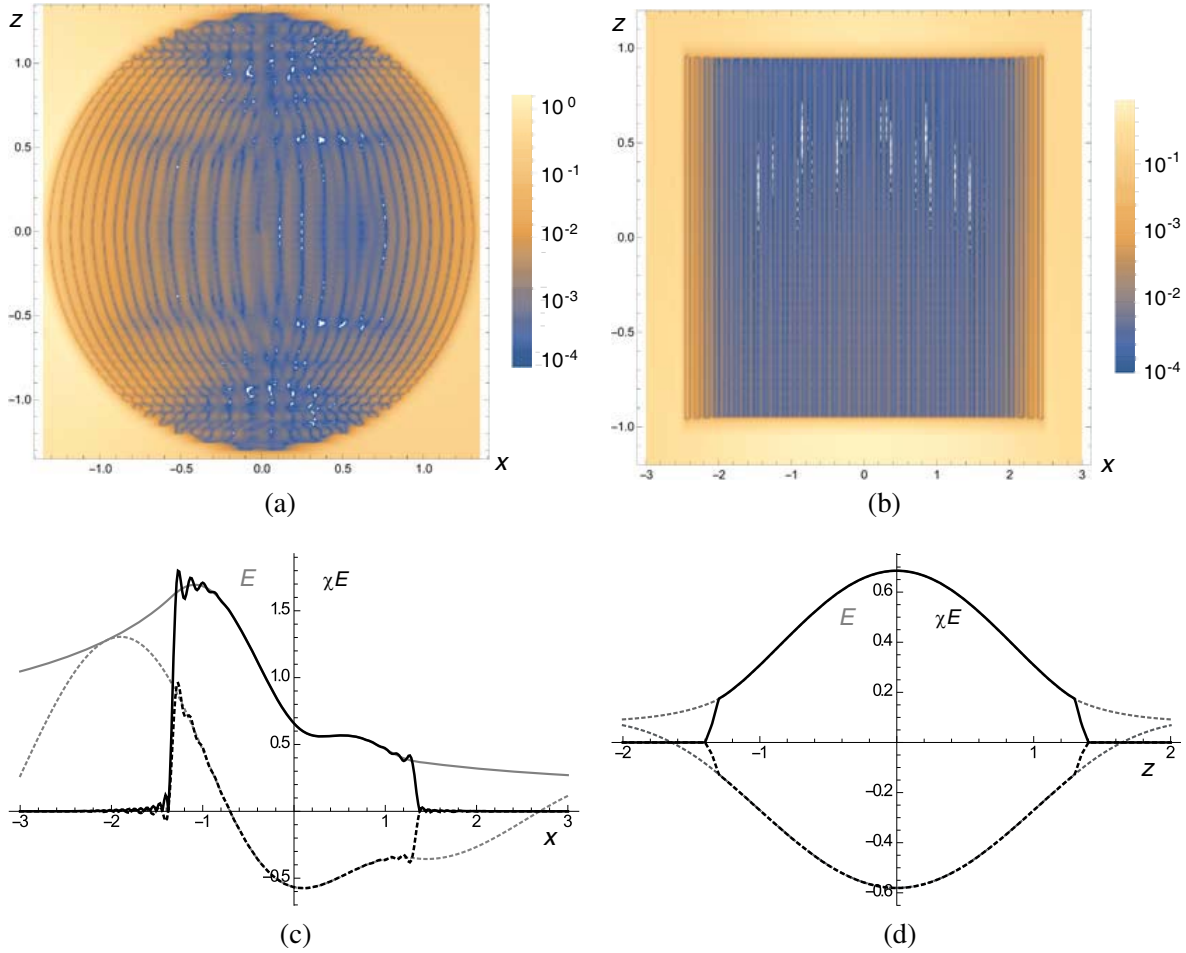


**Figure 7.** In (a) and (b) we plotted the absolute difference (error) between the electric field from the validation  $E$  and  $\chi E$  from our simulation results for the circle resp. the rectangle. At the scatterer these should coincide. In (c) we plotted the real (solid) and imaginary (dotted) part of  $E$  from validation (grey) and  $\chi E$  (black) from our simulation at  $z = -0.2$  for the circle. In (d) we did the same for a vertical cut along  $x = 0$  for the rectangle.

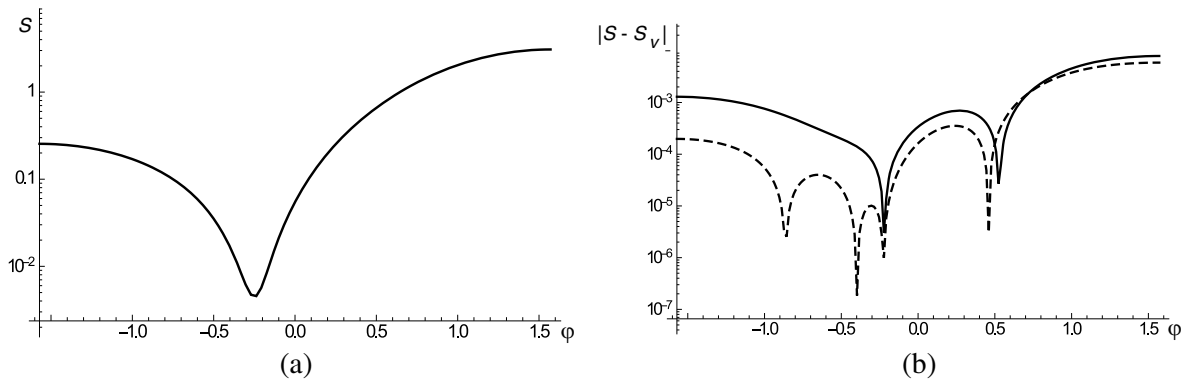


**Figure 8.** (a) The scattering intensity as calculated from the contrast current. (b) The absolute difference between the scattering intensity  $S$  and validation data  $S_V$ , the solid line is with the contrast current from the simulation, the dashed line is with the contrast current from the exact solution, represented by the same discretization as the simulation.

in the contrast source as can be seen in Fig. 7(c). This Gibbs ringing around the discontinuities is not a large problem, since sources with a rapid spatial oscillation do not radiate. In the cut along the line  $x = 0$  (Fig. 7(d)) the simulation and validation overlap very well.

We have also calculated the far-field scattered intensity against the angle as explained in Section 2.4 for the circle. Fig. 8(a) shows the scattering intensity versus the angle. Note that the angle of incidence is  $-\pi/2$  and that the angle is only taken from  $-\pi/2$  to  $\pi/2$  because of the symmetry. In Fig. 8(b) we plotted the error of our simulation results (solid). We also calculated the scattering intensity from the contrast current calculated using the analytic results, but discretized by our discretization. This gives an idea of the maximum reachable accuracy with the given discretization parameters.

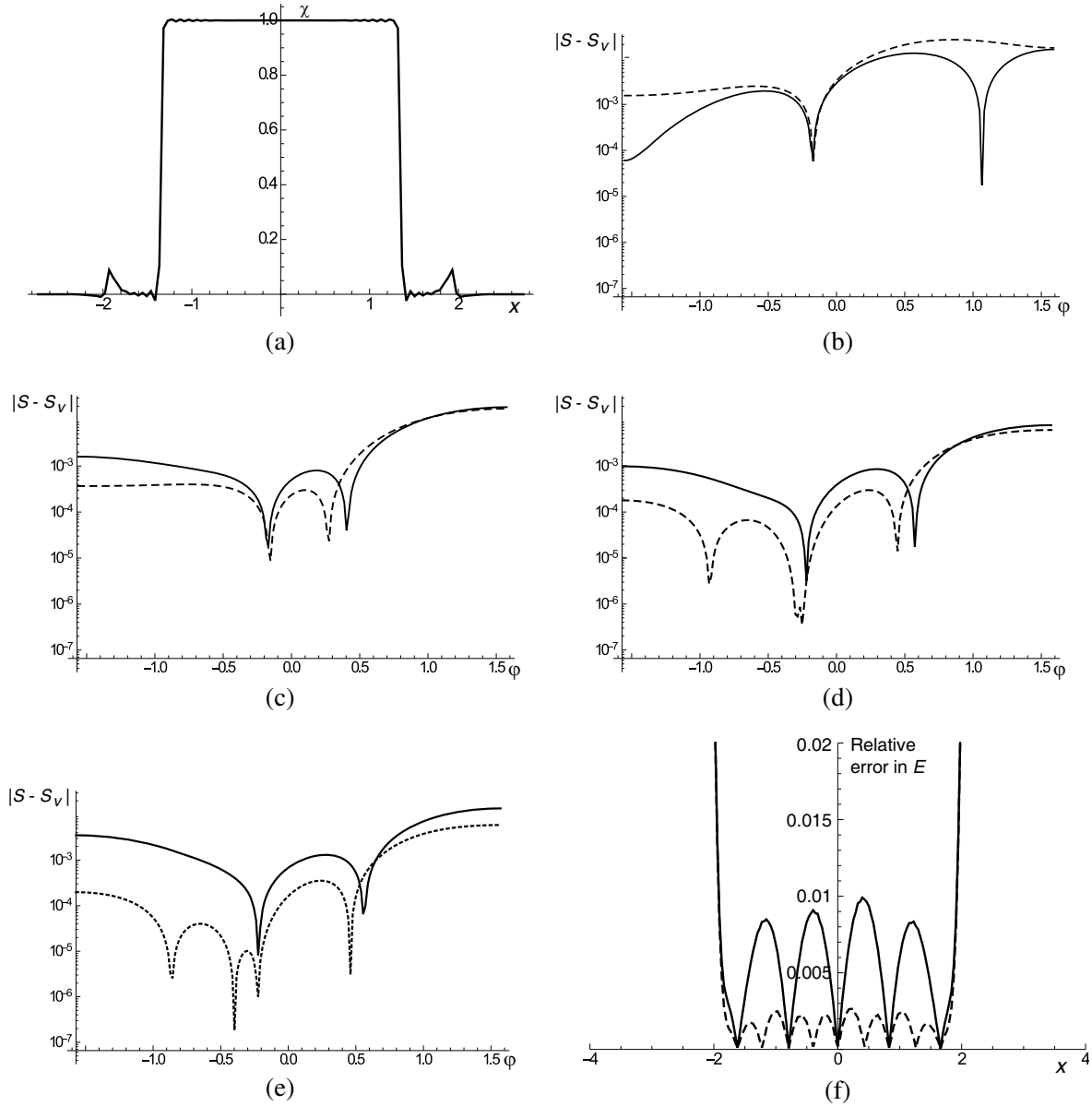


**Figure 9.** In (b), (c), (d) and (e) the solid line depicts simulation error and the dashed line discretization error. (a) The contrast function discretized with 9 windows. (b) The resulting scattering strength error. (c) The scattering strength error with  $\delta = 0.1$ . (d) The scattering strength error with 5 modulation frequencies. (e) The scattering strength error with 8 spatial correction points  $X_\ell$ . (f) Plot of relative error of spectral-spatial transformation, solid:  $\ell \in \{-2, \dots, 2\}$ , dashed:  $\ell \in \{-4, \dots, 4\}$ .

To calculate the scattering intensity we only use that part of the contrast current with a wavenumber smaller than  $k_0$ . This means that most of the current in the spectral domain does not radiate, so it does not contribute, since there are 1.18 Gabor coefficients per unit wavevector.

The spatial sampling in  $x$  is larger than the width of the scatterer, with this Gabor frame  $W \approx 3.5$  for the circle and the rectangle. This is because the Gabor frame needs extra samples at the sides for a good approximation, because the dual window  $\gamma$  (Eq. (18)) is a few times  $X$  wider. This can be seen in Fig. 9(a), which has been created with a low number of spatial windows, so artifacts are visible at the edges. From Fig. 9(b) it is clear that this also yields an increased error for scattering intensity. By simulation error we mean the absolute difference between the calculated scattering strength  $S$  and the validation  $S_V$ , where the absolute value of  $S$  is found in Fig. 8(a). By discretization error we mean the difference between the  $S_V$  and the scattering radiated by the contrast current from our validation data discretized with the indicated settings.

The Gabor coefficients seem to be quite efficient compared to piecewise-linear sampling in the  $z$  direction. When we coarsen the sampling distance in the  $z$  direction from  $\Delta = 0.05$  to  $\Delta = 0.1$  the error in the scattering increases by a factor of three (see Fig. 9(c)). While reducing the number of modulation frequencies does not affect the error in the reflection very much, it does add some (non-radiating) high-frequency noise to the contrast current (see Fig. 9(d)). It seems that the accuracy is limited by the  $z$ -discretization.

We can improve on the interpolation by oversampling in the  $x$  direction. We use 16 times oversampling and making that number smaller increases the error considerably (see Fig. 9(e)). Fig. 9(f) shows the approximation error from approximating an electric field (with magnitude 0.01) with 5 vs.  $9X_\ell$  interpolation points. The location of these  $X_\ell$  values is clearly visible from the dips in the error.

As an example of larger structures that our code is capable of simulating the scattering from, we have included the finite grating structure. From the current distribution in Fig. 10(a) it can be seen that there is a significant mutual coupling between the rectangles in this example. This object is larger than the previous two simulated objects, measuring two by one half wavelength and it shows that our algorithm is useful for larger objects as well. In Fig. 10(b) we can not only identify the first three diffraction orders, we also see scattering at different angles due to the mutual coupling and the finite size of the grating.

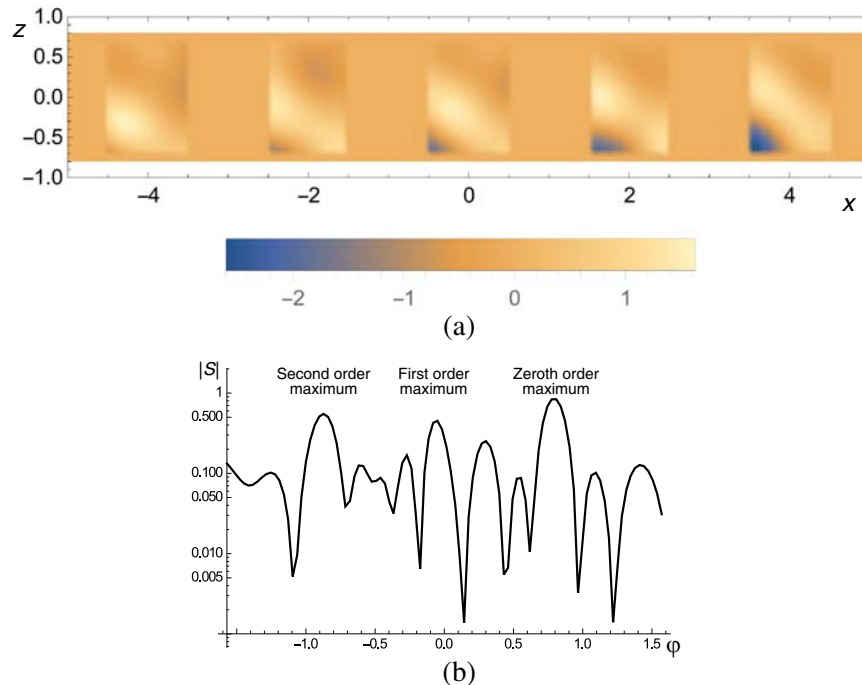


**Figure 10.** (a) The real part of the contrast current density in the grating. (b) The far field scattering intensity from the grating.

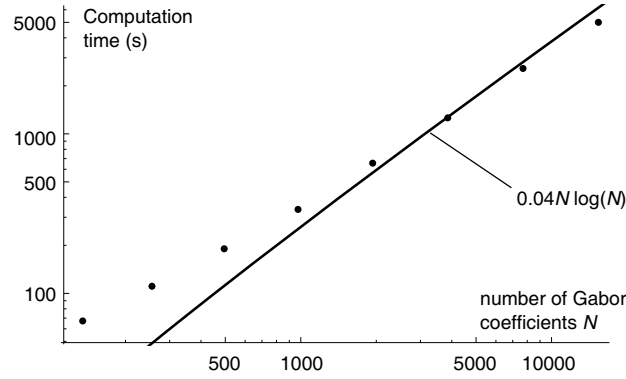


**Figure 11.** Dots indicate computation time of one matrix vector product of operator  $A$  versus the number of Gabor coefficients for an increasing number of modulation frequencies in the Gabor frame. Solid line indicates a reference of  $O(N \log N)$  behaviour.

To show how our code scales to finer discretizations we increased the number of modulation frequencies, the range of  $n$  in (15), several times and measured the time taken for applying the operator  $A$  (Eq. (29)) once, as shown in Fig. 11. The results suggest that the scaling is even better than  $O(N \log N)$ , because  $O(N)$  operations still dominate for this small simulation size. Therefore the  $\log N$  factor will only show up for even higher numbers of Gabor coefficients, where the FFTs will in the end dominate the speed of this operator.

## 6. CONCLUSION

We have constructed an algorithm that solves a 2D domain integral equation for TE polarization in a homogeneous background discretized by a Gabor frame in one direction. The number of numerical operations of this method scales as  $O(N_z N_x \log N_x)$ , with  $N_x$  the number of samples in the  $x$  direction and  $N_z$  the number of samples in the  $z$  direction. The best efficiency is reached in the direction where the Gabor frame was employed. Because of the lower accuracy of the piecewise-linear discretization in the  $z$  direction, more samples per meter are needed in that direction. This clearly shows the value of using the Gabor frame as a discretization.

For every spatial discretization using Gabor frames, there exists a spectral Gabor frame where the individual coefficients are directly mapped onto each other. When we have a spatial discretization of a function with Gabor coefficients, we automatically have a discretization of its Fourier transform. This is very convenient, because the Fourier transform is exact and fast.

With other choices of expansion functions, the Fourier transform is often a difficult step. For example a piecewise-linear discretization creates high-frequency spectral components artificially and the Fourier transform is only an approximation. With the use of a Gabor frame, the most important approximation that we make is the discretization of the problem, the rest can be done (almost) exactly. The downside is that the Gabor frame is not very suitable for discretizing discontinuous (ly differentiable) functions, but, although the spectral Green function is not continuously differentiable, we can work around that by using a coordinate stretch. The method of coordinate stretching is an effective method to cope with the discontinuity of the derivative in  $e^{\gamma|z|}$  and the branchpoints in  $1/\gamma$  simultaneously.

For a discretization with a finer resolution in the  $x$  direction, this method scales very well as  $O(N_x N_z \log N_x)$ . However, a relatively large minimum number of Gabor frames is always needed for small simulation regions.

## ACKNOWLEDGMENT

This research is supported by the Dutch Technology Foundation STW, which is part of the Netherlands Organisation for Scientific Research (NWO), and which is partly funded by the Ministry of Economic Affairs.

## REFERENCES

1. Basharin, A. A., M. Kafesaki, E. N. Economou, C. M. Soukoulis, V. A. Fedotov, V. Savinov, and N. I. Zheludev, "Dielectric metamaterials with toroidal dipolar response," *Physical Review X*, 2015.
2. Ribot, C., P. Lalanne, M.-S.-L. Lee, B. Loiseaux, and J.-P. Huignard, "Analysis of blazed diffractive optical elements formed with artificial dielectrics," *Journal of the Optical Society of America A*, Vol. 24, No. 12, 3819–3826, 2007.
3. Glaser, T., S. Schroter, H. Bartelt, H.-J. Fuchs, and E.-B. Kley, "Diffractive optical isolator made of high-efficiency dielectric gratings only," *Applied Optics*, Vol. 41, No. 18, 3558–3566, 2002.
4. Dzibrou, D. O., J. J. G. M. van der Tol, and M. K. Smit, "Tolerant polarization converter for InGaAsP-InP photonic integrated circuits," *Optics Letters*, Vol. 38, No. 18, 3482–3484, 2013.
5. Wang, L., Y. Wang, and X. Zhang, "Embedded metallic focus grating for silicon nitride waveguide with enhanced coupling and directive radiation," *Optical Express*, Vol. 20, No. 16, 2012.
6. Shlager, K. L. and J. B. Schneider, "A selective survey of the finite-difference time-domain literature," *IEEE Antennas and Propagation Magazine*, Vol. 37, No. 4, 1995.
7. Bengzon, F. and M. G. Larson, *The Finite Element Method: Theory, Implementation, and Applications*, Springer, 2013.
8. Clemens, M. and T. Weiland, "Discrete electromagnetism with the finite integration technique," *Progress In Electromagnetics Research*, Vol. 32, 65–87, 2001.
9. Zwamborn, P. and P. M. van den Berg, "The three-dimensional weak form of the conjugate gradient FFT method for solving scattering problems," *IEEE Trans. Microwave Theory Tech.*, Vol. 40, No. 9, 1992.
10. Bleszynski, E., M. Bleszynski, and T. Jaroszewicz, "AIM: Adaptive integral method for solving large-scale electromagnetic scattering and radiation problems," *Radio Science*, Vol. 31, No. 5, 1225–1251, 1996.
11. Philips, J. R. and J. K. White, "Efficient capacitance extraction of 3D structures using generalized precorrected FFT methods," *IEEE Transactions on Microwave Theory and Techniques*, 253–256, 1994.
12. Botten, I. C., M. S. Craig, R. C. McPhedran, J. L. Adams, and J. R. Andrewartha, "The dielectric Lamellar diffraction grating," *Optica Acta*, Vol. 28, No. 3, 413–428, 1981.
13. Moharam, M. G. and T. K. Gaylord, "Rigorous coupled-wave analysis of planar-grating diffraction," *Journal of the Optical Society of America*, Vol. 71, No. 7, 1981.
14. Chandezon, J., D. Maystre, and G. Raoult, "A new theoretical method for diffraction gratings and its numerical application," *Journal of Optics*, Vol. 11, 235–241, 1980.
15. Poyedinchuk, A. Y., Y. A. Tuchkin, N. P. Yashina, J. Chandezon, and G. Granet, "C-method: Several aspects of spectral theory of gratings," *Progress In Electromagnetics Research*, Vol. 59, 113–149, 2006.
16. Van Beurden, M. C., "A spectral volume integral equation method for arbitrary bi-periodic gratings with explicit Fourier factorization," *Progress In Electromagnetics Research B*, Vol. 36, 133–149, 2012.
17. Pisarenco, M., J. Maubach, I. Setija, and R. Mattheij, "Formulation for simulation of scattering from finite structures," *Journal of The Optical Society of America A*, 2010.
18. Bastiaans, M. J., "A sampling theorem for the complex spectrogram, and Gabor's expansion of a signal in Gaussian elementary signals," *Optical Engineering*, Vol. 20, No. 4, 594–598, 1981.
19. Bastiaans, M. J., "Gabor's expansion and the Zak transform for continuous-time and discrete-time signals: Critical sampling and rational oversampling," Eindhoven University of Technology, Eindhoven, 1995.
20. Feichtinger, H. G. and T. Strohmer, *Gabor Analysis and Algorithms: Theory and Applications*, Birkhauser, 1998.
21. Battle, G., "Heisenberg proof of the Balian-Low theorem," *Letters in Mathematical Physics*, Vol. 15, 175–177, 1988.

22. Benedetto, J. J., C. Heil, and D. F. Walnut, "Differentiation and the Balian-Low theorem," *The Journal of Fourier Analysis and Applications*, Vol. 1, No. 4, 355–402, 1995.
23. Sondergaard, P. L., "Finite discrete Gabor analysis," PhD Thesis, Institut for Matematik, DTU, 2007.
24. Maciel, J. J. and L. B. Felsen, "Discretized Gabor-based beam algorithm for time-harmonic radiation from two-dimensional truncated planar aperture distributions — I: Formulation and solution," *IEEE Transactions on Antennas and Propagation*, Vol. 50, No. 12, 1751–1759, 2002.
25. Maciel, J. J. and L. B. Felsen, "Discretized Gabor-based beam algorithm for time-harmonic radiation from two-dimensional truncated planar aperture distributions — II: Asymptotics and numerical tests," *IEEE Transactions on Antennas and Propagation*, Vol. 50, No. 12, 1760–1768, 2002.
26. Einziger, P. D., S. Raz, and M. Saphira, "Gabor representation and aperture theory," *Journal of the Optical Society of America*, Vol. 3, No. 4, 508–522, 1986.
27. Maciel, J. J. and L. B. Felsen, "Systematic study of fields due to extended apertures by Gaussian discretization," *IEEE Transactions on Antennas and Propagation*, Vol. 37, No. 7, 884–892, 1989.
28. Daubechies, I., S. Jaffard, and J.-L. Journé, "A simple Wilson orthonormal basis with exponential decay," *SIAM Journal on Mathematical Analysis*, Vol. 22, No. 2, 554–572, 1991.
29. Floris, S. J. and B. P. de Hon, "Electromagnetic field expansion in a Wilson basis," *Proceedings of the 42nd European Microwave Conference (EuMC)*, Amsterdam, NL, Oct. 29–Nov. 1, 2012.
30. Lugara, D. and C. Letrou, "Printed antennas analysis by a Gabor frame-based method of moments," *IEEE Transactions on Antennas and Propagation*, Vol. 50, No. 11, 1588–1597, 2002.
31. Jackson, J. D., *Classical Electrodynamics*, Wiley, 2007.
32. Szegő, G., "Orthogonal polynomials," *Royal American Mathematical Society*, 1975.
33. Balanis, C. A., *Advanced Engineering Electromagnetics*, John Wiley & Sons, Inc., 1989.
34. Burger, S., L. Zschiedrich, J. Pomplun, and F. Schmidt, "Finite-element based electromagnetic field simulations: Benchmark results for isolated structures," *Proc. SPIE*, Vol. 8880, 2013.